ELSEVIER

Palaeogeography, Palaeoclimatology, Palaeoecology 188 (2002) 51–71

PALAEO

www.elsevier.com/locate/palaeo

# The mid-Cretaceous water bearer: isotope mass balance quantification of the Albian hydrologic cycle

David F. Ufnar [a,*], Luis A. González [a,b], Greg A. Ludvigson [a,b,c], Robert L. Brenner [a,b], Brian J. Witzke [a,b,c]

[a] *Department of Geoscience, University of Iowa, Iowa City, IA 52242-1379, USA*
[b] *Center for Global and Regional Environmental Research, University of Iowa, Iowa City, IA 52242, USA*
[c] *Iowa Geological Survey Bureau, Iowa City, IA 52242, USA*

Received 5 July 2001; received in revised form 16 August 2002; accepted 30 August 2002

**Abstract**

A latitudinal gradient in meteoric $\delta^{18}O$ compositions compiled from paleosol sphaerosiderites throughout the Cretaceous Western Interior Basin (KWIB) (34–75°N paleolatitude) exhibits a steeper, more depleted trend than modern (predicted) values (3.0‰ [34°N latitude] to 9.7‰ [75°N] lighter). Furthermore, the sphaerosiderite meteoric $\delta^{18}O$ latitudinal gradient is significantly steeper and more depleted (5.8‰ [34°N] to 13.8‰ [75°N] lighter) than a predicted gradient for the warm mid-Cretaceous using modern empirical temperature–$\delta^{18}O$ precipitation relationships. We have suggested that the steeper and more depleted (relative to the modern theoretical gradient) meteoric sphaerosiderite $\delta^{18}O$ latitudinal gradient resulted from increased air mass rainout effects in coastal areas of the KWIB during the mid-Cretaceous. The sphaerosiderite isotopic data have been used to constrain a mass balance model of the hydrologic cycle in the northern hemisphere and to quantify precipitation rates of the equable 'greenhouse' Albian Stage in the KWIB. The mass balance model tracks the evolving isotopic composition of an air mass and its precipitation, and is driven by latitudinal temperature gradients. Our simulations indicate that significant increases in Albian precipitation (34–52%) and evaporation fluxes (76–96%) are required to reproduce the difference between modern and Albian meteoric siderite $\delta^{18}O$ latitudinal gradients. Calculations of precipitation rates from model outputs suggest mid–high latitude precipitation rates greatly exceeded modern rates (156–220% greater in mid latitudes [2600–3300 mm/yr], 99% greater at high latitudes [550 mm/yr]). The calculated precipitation rates are significantly different from the precipitation rates predicted by some recent general circulation models (GCMs) for the warm Cretaceous, particularly in the mid to high latitudes. Our mass balance model by no means replaces GCMs. However, it is a simple and effective means of obtaining quantitative data regarding the mid-Cretaceous hydrologic cycle in the KWIB. Our goal is to encourage the incorporation of isotopic tracers into GCM simulations of the mid-Cretaceous, and to show how our empirical data and mass balance model estimates help constrain the boundary conditions.


*Keywords:* sphaerosiderites; Cretaceous; oxygen isotopes; paleoclimatology; paleosols

* Corresponding author. Present address: Vanderbilt University, Office of Biomedical Research Education and Training, 340 Light Hall, Nashville, TN 37232-0301, USA. Tel.: +1-615-322-3835; Fax: +1-615-343-0749.
*E-mail address:* david.f.ufnar@vanderbilt.edu (D.F. Ufnar).

0031-0182/02/$ – see front matter 
PII: S0031-0182(02)00530-8

## 1. Introduction

The mid-Cretaceous (90–110 Ma) was a time of significantly warmer global temperatures, with atmospheric $CO_2$ concentrations that reached up to 4 times present levels (Barron et al., 1995), and with a more active hydrologic system (Mitchell et al., 1990). Because of the major role that water plays in regulating global temperatures (both as a greenhouse gas and as a source of latent heat), quantifying changes in the hydrologic cycle is critical to a proper understanding of past and future global warming events. Thus, the mid-Cretaceous has received significant attention for assessments and understanding of greenhouse world conditions (e.g. Barron and Peterson, 1990; Barron et al., 1993; Price et al., 1998; White et al., 2001).

The use of sphaerosiderite $\delta^{18}O$ and $\delta^{13}C$ compositions as a paleohydrologic proxy record is a recent development made possible by the recognition of Meteoric Sphaerosiderite Lines (MSLs; Ludvigson et al., 1998). Sphaerosiderites are mm-scale $FeCO_3$ nodules that formed in ancient wetland soil environments (Fig. 1). MSLs are early-diagenetic trends defined by sphaerosiderite isotopic compositions with invariant $\delta^{18}O$ values, and highly variable $\delta^{13}C$ values (Ludvigson et al., 1998). The MSLs are analogous to the meteoric calcite lines of Lohmann (1988). The invariant $\delta^{18}O$ compositions reflect precipitation in a well-developed ground water system of relatively stable $\delta^{18}O$ composition and uniform temperature (Hays and Grossman, 1991; Ludvigson et al., 1998). Hundreds of sphaerosiderite horizons in Albian paleosols in coastal lowland deposits of the Cretaceous Western Interior Basin (KWIB) and North Slope, Alaska (Figs. 2 and 3) have been analyzed to determine the variation in the oxygen isotopic composition of paleoprecipitation over a broad latitudinal range.

Here we report the $\delta^{18}O$ values of meteoric sphaerosiderites from late Albian coastal lowland paleosols in the North American KWIB, which range from −4‰ at 34°N paleolatitude to −16‰ at 75°N. The data presented here expand upon previous reports (Ludvigson et al., 1998; White et al., 2001), and include new locations that provide increased paleolatitudinal coverage. The Albian meteoric $\delta^{18}O$ records we have compiled indicate that meteoric $\delta^{18}O$ values become progressively depleted with increased paleolatitude (Ludvigson et al., 1998; White et al., 2001). Furthermore, the Albian $\delta^{18}O$ latitudinal gradient is steeper than that modeled for siderite forming in modern soil waters. These data challenge any preconceived notions, based on the present-day empirical relationships between surface temperature and precipitation $\delta^{18}O$, that warmer temperatures should result in shallower and heavier $\delta^{18}O$ latitudinal gradients. However, steeper latitudinal precipitation $\delta^{18}O$ gradients should be expected under an intensified hydrologic cycle.

At a global scale, elevated Cretaceous precipitation rates are required by abundant widespread laterites (Sigleo and Reinhardt, 1988), which necessitate precipitation rates in excess of 1000 mm/yr (Bardossy, 1982). In the Western Interior Foreland Basin, features preserved in the mid-Cretaceous stratigraphy require a more active hydrologic cycle. In the eastern margin of the KWIB, widely distributed coarse-grained fluvial deposits required high precipitation rates to produce adequate river discharges to transport these sediments (pebbles and cobbles) from source areas as far away as 1000 km across the stable low-relief sub-continent (Brenner et al., 2000). Moreover, the maximum known westward extent of eastern-sourced Albian clastic deposits suggests tremendous volumes of sediment were being shed from the low-relief eastern sub-continent (Witzke and Ludvigson, 1996; Brenner et al., 2000).

We use the sphaerosiderite data to constrain a mass balance model of isotopic compositions of precipitation to quantify changes in the hydrologic cycle that result in depleted precipitation $\delta^{18}O$ values during greenhouse periods. While our model lacks the complexity of a GCM, it yields results that suggest that earlier general circulation model (GCM) simulations that were unconstrained by paleoprecipitation $\delta^{18}O$ data may have significantly underestimated Cretaceous precipitation rates, in particular at mid to high latitudes. Earlier estimates by our group (White et al., 2001) based on empirical relationships of amount effects for modern monsoonal regions, also produced larger estimated precipitation rates

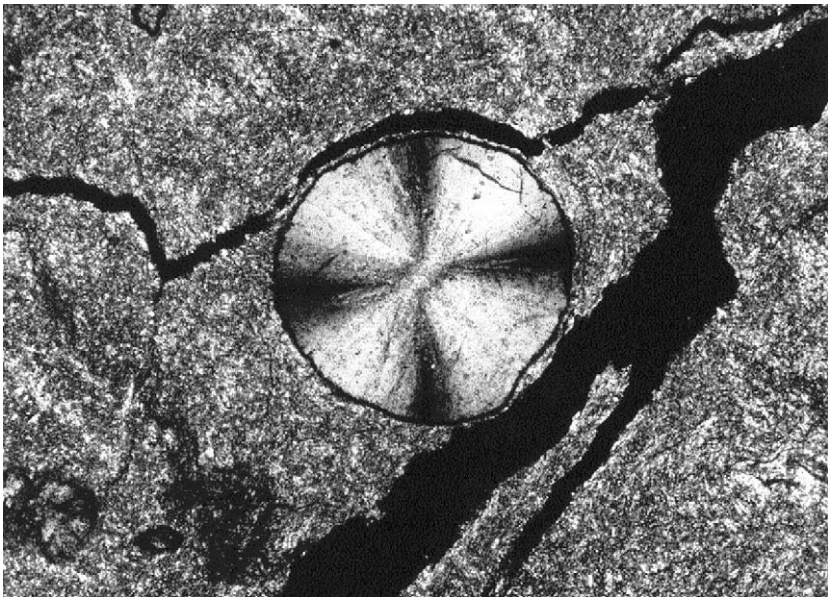

Fig. 1. Cross-polarized light photomicrograph exhibiting a sphaerosiderite nodule contained within a kaolinitic mudstone paleosol of the Boulder Creek Formation of northeastern British Columbia, Canada. Note the characteristic pseudo uniaxial cross-extinction pattern resulting from the nodule's radial concentric crystalline microstructure (field of view is 1.3 mm in length).

for the mid-latitudes of the KWIB eastern margin. The technique used by White et al. (2001), however, cannot be applied over the full latitudinal range of the northern hemisphere.

## 2. Methods

Sphaerosiderite-bearing paleosols have been sampled throughout the KWIB, and the best specimens have generally been obtained from cores and active quarries as the sphaerosiderites rapidly oxidize when exposed in outcrops (Fig. 2). The lower-latitude samples (34–35°N paleolatitude) were primarily obtained from cores and clay pits in the Dakota Formation of western Iowa (e.g. Sioux City Brick Co.), southeastern Nebraska (Yankee Hill Brick and Tile Co.), Kansas (Kansas Geological Survey Jones #1 and Kenyon #1 Cores, the Amoco Rebecca Bounds Core), and outcrops of the Dakota Formation of Utah (White et al., 2001). The mid-latitude samples (35–50°N paleolatitude) were obtained from outcrops of the Swan River Formation in the area of the Manitoba escarpment (southeastern Saskatchewan and southwestern Manitoba) (Ludvigson et al., 1998), cores of the Swan River Formation of southeastern Saskatchewan (Saskatchewan Geological Survey Yarbo Core), and cores of the Mattagami Formation from the Moose River Basin of Ontario (Ontario Geological Survey, cores: OGS 84-06 and OGS 84-08) (White et al., 2000a). Samples of the Mannville Group, Success S2 Formation from southern Alberta (Shell Mayberries Core 16-4-6-5w4, Alberta Energy and Utilities Board Core Research Center (AEUB), Calgary, AB, Canada) were donated by Dr. Dale Leckie. Samples were also obtained from the Bow Island Formation of southern Alberta (Melaar Kipp Core, 6-32-10-22w4, AEUB) (McCarthy et al., 1997). The higher-latitude samples (50–75°N paleolatitude) were obtained from the Boulder Creek Formation of northeastern British Columbia (MD 80-08 coal exploration core, Geological Survey of Canada Core Research Facility, Calgary, AB, Canada), and the Paddy Member of the Peace River Formation in northwestern Alberta (Amoco et al. Wapiti wells 10-11-69-9w6

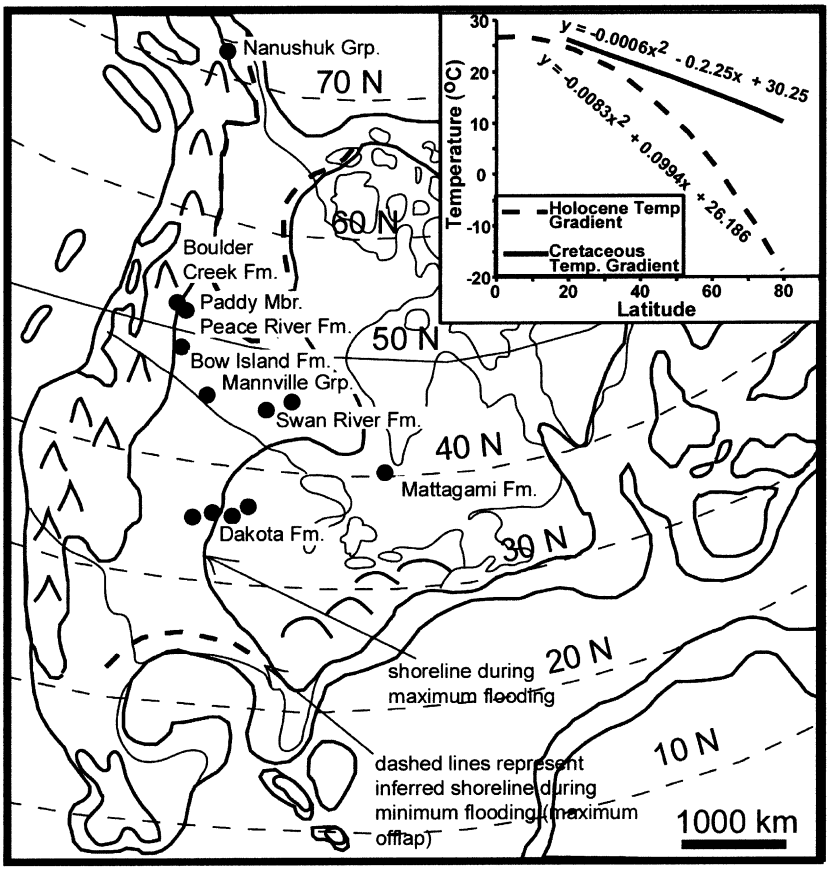


Fig. 2. Aptian–Albian paleogeographic reconstruction of North America (modified from Scotese, 1991), illustrating sampling locations for the sphaerosiderite-bearing paleosols ranging from 34°N paleolatitude to 75°N. Inset graph illustrates the latitudinal temperature profiles of Spicer and Corfield (1992) with best-fit polynomial equations. These equations were used to describe the latitudinal distribution of temperature in the modeling experiments.

and 10-32-69-8w6 and the Sulpetro et al. well 14-14-69-9w6, AEUB, Calgary, AB, Canada). Samples from the North Slope, Alaska were recovered from the Corwin Formation of the Nanushuk Group (Grandstand #1 Core, USGS Core Research Center, Denver, CO, USA).

Sphaerosiderite-bearing paleosol samples are petrographically analyzed to isolate unaltered, early-diagenetic siderite using polarized light, cathodoluminescence, epifluorescence, and scanning electron microscopy. Unaltered sphaerosiderites are microsampled using a microscope-mounted dental drill with a 0.5 mm bit. No less than 10 microsamples were obtained from each sphaerosiderite-bearing paleosol for isotopic analyses. Samples extracted for mass spectrometry were analyzed at either the University of Iowa Paul H. Nelson Stable Isotope Laboratory or the University of Michigan Stable Isotope Laboratory. Powdered samples are vacuum-roasted at 380°C for 1 h, then reacted with anhydrous phosphoric acid at 72°C for approximately 15 min in a Kiel III automated carbonate reaction device connected to a Finnigan MAT 252 (Iowa) or MAT 251 (Michigan) ratio mass spectrometer. All isotopic values are reported relative to the PeeDee Belemnite (PDB) standard, with analytical precision of better than ±0.05‰ for both carbon and oxygen. Interlaboratory comparisons of selected samples yielded consistent results (e.g. Boulder

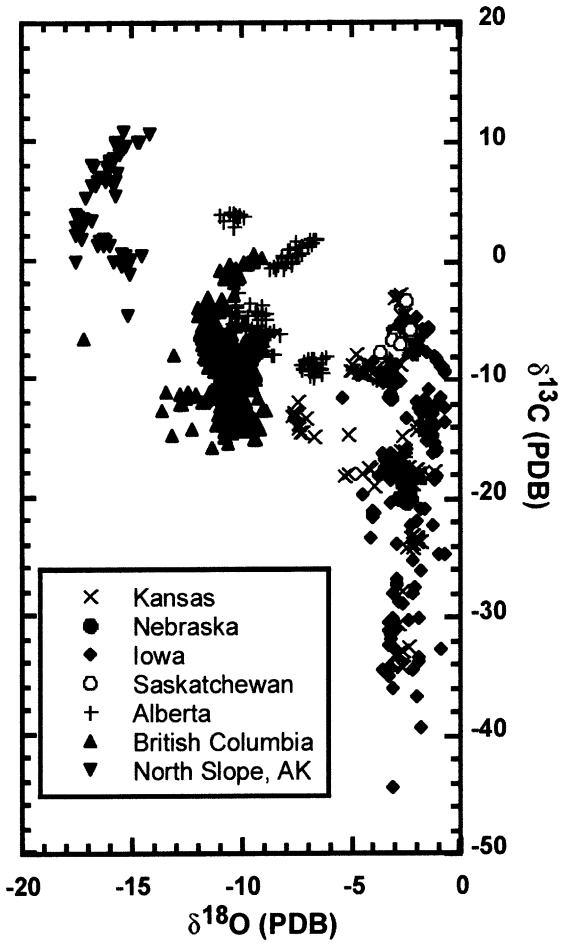


Fig. 3. Compiled meteoric sphaerosiderite $\delta^{18}O$ vs. $\delta^{13}C$ data from throughout the KWIB and the North Slope of Alaska. A total of 910 analyses are illustrated in this graph, and 550 of these from Alberta (Peace River Formation), British Columbia (Boulder Creek Formation), and North Slope, Alaska (Nanushuk Group) are new analyses not presented in Ludvigson et al. (1998) and White et al. (2001). Analyses from individual horizons are not denoted on this illustration. For detailed analyses of individual sphaerosiderite-bearing horizons, readers are referred to Ludvigson et al. (1998), Ufnar et al. (2001), and White et al. (2000a). See text for more information concerning the locations of sample sites. The averages for individual sphaerosiderite-bearing horizons are plotted on the gradient illustrated in Fig. 4.

Creek Formation analyses). The siderite data are corrected to account for the temperature-dependent isotope fractionation between siderite and phosphoric acid using the relationship of Carothers et al. (1988).

## 3. Latitudinal gradients in meteoric siderite $\delta^{18}O$ compositions

### 3.1. A predicted mid-Cretaceous meteoric siderite $\delta^{18}O$ paleolatitudinal gradient

Modern studies of evolving water vapor in air masses show a correlation exists between mean annual surface temperature and the weighted mean annual oxygen isotopic composition of precipitation (Dansgaard, 1964; Yurtsever and Gat, 1981; Rozanski et al., 1993; Clark and Fritz, 1997). On a global scale, Dansgaard (1964) and Dansgaard et al. (1973) established a linear relationship between surface air temperatures and the $\delta^{18}O$ of mean annual precipitation:

$$\delta^{18}O = 0.695T_{annual} - 13.6‰ \text{ SMOW}$$

(Dansgaard, 1964)

$$\delta^{18}O = 0.620T_{annual} - 15.25‰$$

SMOW (Dansgaard et al., 1973)

Using the temperature–$\delta^{18}O$ precipitation relationship of Dansgaard et al. (1973), and the empirical warm Cretaceous temperature gradient of Wolfe and Upchurch (1987), we have calculated an expected Albian meteoric siderite $\delta^{18}O$ gradient (Fig. 4). The expected gradient predicts values of +1.3‰ at 35°N latitude and −2.6‰ at 75°N latitude, and the equation for the slope of the curve is shown in Fig. 4. The empirical Albian sphaerosiderite $\delta^{18}O$ latitudinal trend is 5.8‰ (34°N) to 13.8‰ (75°N) lighter than is predicted for the mid-Cretaceous (Fig. 4) using the modern empirical temperature–$\delta^{18}O$ relationships (Dansgaard, 1964; Dansgaard et al., 1973).

### 3.2. Theoretical modern meteoric siderite $\delta^{18}O$ latitudinal gradient

To make comparisons with modern siderite $\delta^{18}O$ gradients, and calibrate the mass balance model to present-day conditions, we used the International Atomic Energy Agency (IAEA)/World

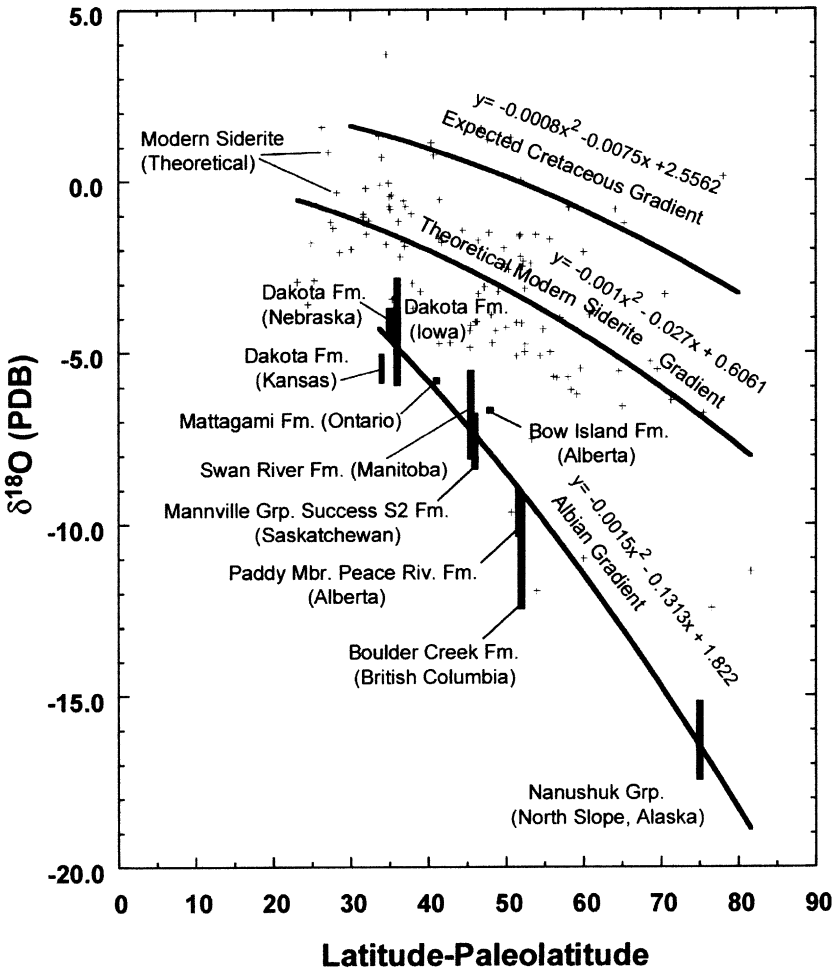


Fig. 4. Graph comparing the Albian sphaerosiderite $\delta^{18}O$ latitudinal gradient, the modern (calculated) siderite $\delta^{18}O$ gradient, and the expected warm Cretaceous siderite gradient calculated from the modern temperature–$\delta^{18}O$ relationship of Dansgaard (1964). The Albian trend has significantly lower $\delta^{18}O$ values and a steeper latitudinal gradient than both the modern and predicted mid-Cretaceous gradients. The modeled modern siderite compositions were calculated using IAEA/WMO data (Rozanski et al., 1993), and the experimentally determined siderite fractionation factor of Carothers et al. (1988). The vertical lines on the Albian empirical gradient represent the range of average $\delta^{18}O$ values (MSLs) obtained from individual sphaerosiderite-bearing paleosol horizons for that paleolatitude. For example, the Boulder Creek Formation line represents the range of average $\delta^{18}O$ values obtained from 30 separate sphaerosiderite-bearing paleosols (with 10 analyses performed on each horizon).

Meteorological Organization (WMO) data published in Rozanski et al. (1993). From the IAEA/WMO precipitation isotopic compositions we calculated a theoretical modern siderite $\delta^{18}O$ latitudinal gradient (Fig. 4). We have interpreted the Albian sphaerosiderite-bearing paleosols to have formed in lowland, fluvial/estuarine coastal plane paleoenvironments (Ludvigson et al., 1998; White et al., 2000b). Thus, to obtain the most analogous contemporary siderite $\delta^{18}O$ compositions, we filtered the IAEA/WMO data (Rozanski et al., 1993) to include only those stations that occur at low elevations ($< 300$ m above sea level), with minimal local precipitation amount effects. As expected with cooler global temperatures, the calculated modern siderite $\delta^{18}O$ latitudinal gradient is more depleted than the predicted warm-Cretaceous siderite $\delta^{18}O$ latitudinal gradient (Fig.

3). However, the calculated modern gradient is 3.0‰ (35°N latitude) to 9.7‰ (75°N) heavier than the empirical Albian sphaerosiderite $\delta^{18}O$ paleolatitudinal gradient (Fig. 4). The contrast between the predicted mid-Cretaceous siderite $\delta^{18}O$ latitudinal gradient, based upon the modern empirical temperature–$\delta^{18}O$ precipitation relationships of Dansgaard (1964), and our empirical sphaerosiderite $\delta^{18}O$ paleolatitudinal gradient was the impetus for the mass balance modeling experiments presented below.

We have suggested that increased precipitation and greater global rainfall (amount effects) could account for steeper Mesozoic meteoric $\delta^{18}O$ gradients (Ludvigson et al., 1998). Similarly, during the warm equable Eocene, increased rainout effects are a suspected cause for lighter meteoric $\delta^{18}O$ compositions recorded in fossil vertebrate teeth (Koch et al., 1995). White et al. (2001) applied the well-established modern precipitation amount–$\delta^{18}O$ relationship (Dansgaard, 1964) to a subset of our empirical sphaerosiderite data to make estimates of precipitation rates on the eastern margin of the KWIB. The results of White et al. (2001) show high precipitation rates on the eastern margin of the KWIB (2500–4100 mm/yr). However, considering the disparity between the predicted and empirical mid-Cretaceous siderite $\delta^{18}O$ gradients, there are some concerns with applying modern-day empirical relationships that are controlled by the present-day temperature gradient (i.e. modern climate) to ancient systems with very different climatic regimes. Thus, we have opted to use a mass balance approach that does not rely on modern-day empirical relationships, to model precipitation fluxes and simulate the latitudinal distribution of Albian meteoric $\delta^{18}O$ values. Here we explore and quantify the causes for the observed paleolatitudinal $\delta^{18}O$ trend using a mass balance model constrained by meteoric $\delta^{18}O$ values obtained from mid-Cretaceous sphaerosiderites.

## 4. Mass balance model

Our mass balance model tracks the evolving isotopic composition of an air mass and its precipitation, and is driven by latitudinal temperature gradients. It differs from a simple Rayleigh distillation model in that it accounts for vapor feedback from oceans and land, and incorporates humidity-controlled kinetic effects. The premise of our mass balance model is that air masses develop and acquire moisture in tropical–subtropical regions, and lose moisture through precipitation during poleward migration. The air mass vapor is progressively removed through precipitation and replenished through evaporation. The model tracks the $\delta^{18}O$ of vapor in the air mass using the following mass balance equation:

$$\delta^{18}O_{a(n)} = \frac{\left[\delta^{18}O_{a(n-1)} \cdot f_{(n-1)} + \left(\delta^{18}O_v \cdot \frac{de}{dt} - \delta^{18}O_r \cdot \frac{dr}{dt}\right)\right]}{\left[f_{(n-1)} - \frac{de}{dt} + \frac{dr}{dt}\right]} \quad (1)$$

$\delta^{18}O_{a(n)}$ = composition of water vapor in the air mass,

$f$ = fraction of vapor remaining in the vapor reservoir,

$\delta^{18}O_v$ = composition of vapor added via evaporation,

$de/dt$ = vapor fraction added through evaporation (vapor flux),

$\delta^{18}O_r$ = composition of precipitation removed from the air mass,

$dr/dt$ = vapor fraction removed through precipitation (precipitation flux).

The compositions of vapor added and precipitation removed from the air masses are determined by latitudinal temperature gradients, temperature-dependent water vapor isotopic fractionation factors (Majoube, 1971), and the compositions of marine and terrestrial source waters. To reduce uncertainties in estimating vapor content of the air masses, the model tracks yearly fluxes as dimensionless fractions relative to the air mass vapor content. The fluxes enrich (increase $\delta^{18}O$ values) and deplete (decrease $\delta^{18}O$ values) the isotopic composition of vapor in an atmospheric reservoir that was arbitrarily set to

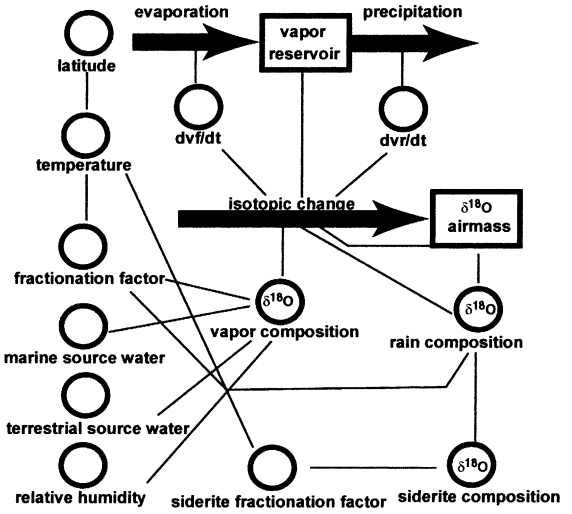


Fig. 5. Schematic illustration of the mass balance model components. The model was constructed using Stella® 6.0 Research software by High Performance Systems, Inc. The boxes represent 'reservoirs', the circles are 'converters', and the arrows represent 'flows'. The relative humidity, marine source water, terrestrial source water, precipitation flux, and evaporation flux converters are all graphical functions that can be manually changed by model operators during simulations. The polynomial equations for the latitudinal temperature gradients (Fig. 1) are embedded in the converter labeled 'temperature'. The mass balance equation (Eq. 1 in text) is embedded in the flow labeled 'isotopic change'. The 'siderite fractionation factor' converter contains the temperature-dependent equation for siderite of Carothers et al. (1988). The 'vapor reservoir' was set to an initial value of 1, and the 'air mass vapor' reservoir was set to the calculated initial isotopic composition of vapor with a marine source at 0° latitude. The equation for the kinetic effects of relative humidity (Gonfiantini, 1986) (Eq. 2 in text) is contained in the converter labeled 'vapor composition'.

a value of 1, representing the initial amount of water vapor (Fig. 5). With each incremental step in latitude, a fraction of the atmospheric water is removed through the precipitation flux and replenished via the evaporation flux. The isotopic composition of each component (newly evaporating water vapor, air mass vapor, and precipitation) is recalculated with each latitudinal step.

Several assumptions were made in creating this model. First, we assume that the fractionation factors for siderite derived by Carothers et al. (1988) apply over the whole range of sedimentary temperatures, an assumption supported by the theoretical work of Zheng (1999). Second, we assume that the sphaerosiderite $\delta^{18}O$ compositions (MSLs) reflect precipitation in shallow groundwater systems where groundwater temperatures are at the mean annual temperatures (MATs) of that particular location (Liu et al., 1995). This is a significant assumption discussed in detail by White et al. (2001). The time necessary for well-developed, mm-scale sphaerosiderites to form is unknown; however, we believe that $10^2$–$10^4$ yr is likely. If seasonal variations are recorded in the sphaerosiderites (perhaps at the μm scale), our sampling procedures homogenize any seasonal $\delta^{18}O$ trends. Groundwaters sampled below the water table, however, generally have isotopic compositions that are very similar to the weighted average of precipitation (Clark and Fritz, 1997). Furthermore, in fine-grained soils (e.g. kaolinitic mudstone paleosols) the critical depth where the isotopic composition of the ground/soil water is attenuated to the weighted mean average annual precipitation $\delta^{18}O$ is relatively shallow ($<0.50$ m) (Liu et al., 1995). Third, we assume no seasonal biases in the local groundwater recharge (Clark and Fritz, 1997). If there were seasonal biases in the soil groundwater compositions, then our precipitation rate calculations might represent maximum possible values. In order to evaluate the local variability in meteoric $\delta^{18}O$ compositions, multiple sphaerosiderite-bearing paleosols (where available) were sampled to best characterize temporal trends in sphaerosiderite $\delta^{18}O$ compositions for that particular location (paleolatitude). Fourth, our model treats all precipitation as liquid and assumes no isotopic compositional variations between liquid and solid (hail and snow) precipitation. Fifth, the model treats fresh surface water bodies, soil water, and evapotranspiration as a single terrestrial source with latitudinally variable $\delta^{18}O$ compositions. Sixth, our model is only constrained between 34° and 75°N paleolatitude. Increased latitudinal coverage (particularly in low latitudes) could change the modeled fluxes and consequently the estimated precipitation rates.

We calibrated the model to present-day conditions using the IAEA/WMO precipitation and temperature data (Rozanski et al., 1993), to produce the calculated modern (theoretical) siderite

Table 1
The tabulated information outlines the procedure that was followed to derive modern theoretical sphaerosiderite $\delta^{18}O$ values from modern meteoric water (shallow groundwater) $\delta^{18}O$ values

| Step | Procedure |
|---|---|
| 1 | The first step is to obtain $\delta^{18}O$ precipitation values and MAT values from low altitude, coastal IAEA/WMO recording stations (Rozanski et al., 1993) |
| 2 | Next, the temperature-dependent fractionation factor ($\alpha$) is calculated using the following formula: $\exp(3.13\times10^6/T^2 - 3.5)$ (with $T$ in K) (Carothers et al., 1988) |
| 3 | Then, use $\alpha$ to find the $\delta^{18}O_{siderite}$ value in ‰ SMOW using the following formula: $((\alpha(\delta^{18}O_{precipitation}+1000))-1000)$ |
| 4 | Finally, convert the $\delta^{18}O_{siderite}$ value to ‰ PDB using the following conversion formula: $((\delta^{18}O_{siderite}\ (SMOW) - 30.86)/1.03086)$ |

$\delta^{18}O$ latitudinal gradient. We filtered the Rozanski et al. (1993) data set to include only those stations located at low elevations (< 300 m), and locations free of monsoons (amount effects). The weighted average $\delta^{18}O$ ppt values from these stations were then used to estimate theoretical siderite $\delta^{18}O$ values for that particular latitude using the methods outlined in Table 1. For modern simulations, we set the marine $\delta^{18}O$ composition at 0‰ (SMOW). The modern model simulations were also tuned to replicate present-day evaporative flux and northern hemisphere latitudinal precipitation distribution (Barron et al., 1989; Gates et al., 1992).

Temperature gradients were obtained from modern average equator-to-pole temperature distributions (for modern model simulations). The empirical warm Cretaceous temperature gradient of Wolfe and Upchurch (1987) was used for Albian model simulations. The temperature gradients were fitted with second-order polynomial equations (Fig. 2), enabling the model to calculate temperature as a function of latitude. Alternative latitudinal temperature profiles generated from mid-Cretaceous GCM paleoclimatological experiments were also embedded in the model to test model sensitivity to changing temperature gradients.

Computation of the vapor feedback composition to the air masses incorporates a latitudinally variable relative humidity function. The kinetic effects of humidity were tracked using the following relationship of Gonfiantini (1986):

$$\Delta\varepsilon^{18}O_{bl-v} = 14.2\cdot(1-h)\ ‰ \quad (2)$$

(bl = boundary layer, v = vapor, $h$ = humidity, $\varepsilon = (\alpha - 1)\times10^3$)

The latitudinal distribution of relative humidity is a model input with a sinusoidal curve that can be reconfigured for model simulations. Peaks in the curve correspond to humid latitudinal belts and troughs the dry belts. The relative humidity curve was initially modeled (then tested) to simulate the modern global distribution (average) of relative humidity in marine/coastal areas (NOAA, 2001).

For Albian simulations, we set the $\delta^{18}O$ composition of Tethyan Ocean source water at −1.2‰ (SMOW)(Shackleton and Kennett, 1975; Dettman and Lohman, 2000). The marine source water $\delta^{18}O$ composition was then varied (see sensitivity tests below) to see how changing marine source water compositions might affect model outputs. Simulations were also performed varying the contributions of marine-derived vapor feedback from 60 to 100% (i.e. terrestrial-derived source water from 40 to 0%). Albian terrestrial-source water isotopic compositions were estimated from the sphaerosiderite $\delta^{18}O$ gradient and were also tested in the following sensitivity experiments.

## 5. Sensitivity tests

Once the model was satisfactorily calibrated to reproduce the modern (theoretical) siderite $\delta^{18}O$ latitudinal gradient, adjustments in the model input parameters were made in order to reproduce the empirical Albian sphaerosiderite $\delta^{18}O$ paleolatitudinal gradient. The first adjustment was to change the equator-to-pole temperature gradient from the modern to the empirical warm Cretaceous gradient of Wolfe and Upchurch (1987). Then, the marine and terrestrial source water $\delta^{18}O$ values were adjusted to interpreted mid-Cretaceous values (see below). The relative humidity

Table 2
Summary of sensitivity tests performed on the various input parameters of the mass balance model

| Parameter | Run 1 | Run 2 | Run 3 | Run 4 | Run 5 | Run 6 |
|---|---|---|---|---|---|---|
| Relative humidity | 0°: 96%, 50°: 90%, 10°: 95%, 60°: 87%, 20°: 73%, 70°: 82%, 30°: 60%, 80°: 90%, 40°: 75%, 90°: 95% | RH was decreased 5–8% from 0 to 20°N lat., increased 10% from 25 to 35°, and same as Run 1 from 40 to 90° | RH was held nearly constant w/latitude oscillating 2–3% about a mean value of 81% | RH was decreased 15% from 0 to 15°, 5% from 15 to 25°, 8% from 25 to 30°, same as Run 1 from 35 to 40°, decreased 12–15% from 40 to 90° | RH was decreased by 20% from 0 to 20°, 40% from 25 to 35°, 25% from 40 to 90° | RH values increased 3–5% from 0 to 15°, 2–3% from 15 to 20°, 20% from 25 to 25°, 8–10% from 40 to 80°, 2–3% from 80 to 90° |
| $\delta^{18}O$ composition of the KWIS surface waters (SMOW) | seaway composition was held constant at a $\delta^{18}O$ value of −1.2‰ (SMOW) | from 0 to 35° the seaway $\delta^{18}O$ values were enriched by up to 2.0‰ w/a peak at 10° (0.8‰), from 35 to 90° the seaway values were depleted by up to 1.7‰ w/lowest values reaching −3.0‰ at 60° | from 0 to 30° the seaway $\delta^{18}O$ values were enriched by up to 4‰ w/a peak at 10° (2.8‰), from 30 to 90° the seaway values were depleted by up to 2.8‰ w/lowest values reaching −4‰ at 60° | seaway $\delta^{18}O$ values were held constant at −4‰ from 0 to 50°, then increased steadily to +2.0‰ from 50 to 90° | seaway $\delta^{18}O$ values decreased steadily from +2.5‰ at 0° to −4.0‰ at 30°, remained constant at −4.0‰ from 30 to 50°, then increased from −4.0‰ to 0‰ from 50 to 90° | seaway $\delta^{18}O$ values increased steadily from −4.0‰ at 0° to +4.0‰ at 50°, then decreased steadily from +4.0‰ at 50° to a minimum value of −4.5‰ at 90° |
| $\delta^{18}O$ composition of continental source water (SMOW) | the $\delta^{18}O$ gradient becomes increasingly depleted w/increased latitude, 0°: +3.0‰, 30°: −4.0‰, 60°: −14.0‰, 90°: −27.0‰ | continental source water $\delta^{18}O$ values are enriched relative to Run 1 w/a shallower gradient, 0°: +5.0‰, 90°: −5.0‰ | continental source water $\delta^{18}O$ values are more depleted values and have a steeper gradient relative to Run 1, 0°: −4.0‰, 90°: −47.0‰ | continental source water compositions were modeled with a highly depleted, exponential gradient w/$\delta^{18}O$ values of −25.0‰ at 0° and −45.0‰ at 90° | $\delta^{18}O$ values increase from −7.0 to +5.0‰ from 0 to 30°, then decrease from +5.0 to −28.0‰ from 30 to 70°, decrease from −28.0 to −32.0‰ from 70 to 90° | $\delta^{18}O$ values increase from −5.0 to +3.0‰ from 0 to 30°, then decrease from +3.0 to −10.0‰ from 30 to 60°, between 65–90° the $\delta^{18}O$ values are constant at −12‰ |
| Precipitation flux | 0°: 1.0; 50°: 0.50, 10°: 0.25, 60°: 0.33, 20°: 0.09, 70°: 0.20, 30°: 0.18, 80°: 0.14, 40°: 0.50, 90°: 0.14 | precipitation flux was increased 55% at 10°, 15% at 20°, 10% at 30°, 12% at 40°, 10% from 50 to 60°, 20% from 70 to 90° | precipitation flux was increased 65% at 10°, 38% at 20°, 40% at 30°, 30% at 40°, 25% at 50°, 15% at 60°, 20% at 70°, 23% from 80 to 90° | precipitation flux was decreased by 28% at 0°, 15% at 10°, 5% at 20°, 3% at 30°, 5% at 40°, 10% from 50 to 90° | precipitation flux was decreased by 40% at 0°, 18% at 10°, 10% from 20 to 30°, 15% from 40 to 90° | precipitation flux was modeled with a steady decline from an initial value of 0.88 at 0° to a final value of 0.18 at 90° |
| Evaporation flux | 0°: 1.0, 50°: 0.50, 10°: 0.25, 60°: 0.33, 20°: 0.09, 70°: 0.20, 30°: 0.18, 80°: 0.14, 40°: 0.50, 90°: 0.14 | evaporation flux was increased 20% at 0°, 25% at 10°, 35% at 20°, 40% at 30°, 20% at 40°, 10% at 50°, 5% at 60°, same as Run 1 from 70 to 90° | evaporation flux was modeled with an exponential decline from an initial value of 0.90 at 0° to a final value of 0.01 at 90° | evaporation flux was decreased 15% at 0°, 22% at 10°, 30% at 20°, same as Run 1 at 30°, increased by 25% from 40 to 60°, 20% at 70°, 15% from 80 to 90° | evaporation flux was increased by 13% at 0°, 10% at 10°, 5% at 20°, 42% at 30°, 20% from 40 to 50°, 45% at 60°, and 20% from 70 to 90° | evaporation flux was decreased 20% at 0°, 25% at 10°, increased by 20% at 30°, 15% at 40°, 10% at 50°, 22% at 60°, 15% at 70°, 10% from 80 to 90° |

For each model input parameter, the Run 1 settings reproduce an Albian latitudinal gradient that is identical to the polynomial regression illustrated in Fig. 4. In Runs 2–6 changes are either described relative to the Run 1 settings, or the values have been tabulated.

profile was held constant to that of the modern northern hemisphere since we have no basis upon which to make changes. Finally, we adjusted the precipitation and evaporation flux curves until the modeled siderite $\delta^{18}O$ gradient approached our empirical values. The input parameters were adjusted until the model produced a curve statistically identical ($R^2 > 0.95$) to the polynomial fit of the empirical sphaerosiderite data over the sampled latitudinal range (35–75°N paleolatitude). Numerous simulations were made to test model sensitivity to changes in various parameters and to determine which exerted greater control on the calculated latitudinal gradients (Table 2). The sensitivity experiments determined model responses to changes in: (a) relative humidity, (b) marine source water $\delta^{18}O$ compositions, (c) continental source water $\delta^{18}O$ compositions, (d) evaporative feedback flux, (e) precipitation flux, and (f) temperature. The results of sensitivity experiments are shown in Figs. 6–8. For the tests illustrated in Fig. 6, six trials or 'Runs' were made with Run 1 representing the settings that replicate the empirical Albian sphaerosiderite $\delta^{18}O$ latitudinal gradient. When testing the various input parameters, the remaining variables were held constant at the 'Run 1' (best-fit) settings.

### 5.1. Relative humidity

Changing the average relative humidity over all latitudes and the amplitude of variation between humid and dry belt regions were used to test the model sensitivity to changes in relative humidity. Runs 1–3 (Fig. 6A,B) generate siderite $\delta^{18}O$ values that closely resemble the empirical Albian latitudinal gradient in meteoric sphaerosiderite $\delta^{18}O$ compositions, with Run 1 representing the best fit. In Run 1, the tropical (0–20°N), mid-latitude (35–60°N), and polar latitudes (80–90°N) are characterized by high relative humidity in the range of 90–95%. In Run 1, the dry belt (20–35°N) relative humidity is in the range of 55–60%. Run 2 is similar to Run 1, but differs in that the dry belt regions (20–35°N) were modeled with relative humidity in the range of 70–75%. Run 3 was intended to test the model sensitivity to a nearly invariant latitudinal distribution of relative humidity with an average value of approximately 81% (Fig. 6A,B). Run 4 was set to simulate a latitudinal distribution in relative humidity that is similar to the average modern distribution over the Pacific Ocean (NOAA, 2001). This trend shifted the simulated siderite $\delta^{18}O$ gradient to slightly more depleted (1–2‰) values. Run 5 simulates more extreme, low equator-to-pole relative humidity values, and results in a simulated siderite $\delta^{18}O$ gradient that is depleted by 3–4‰ relative to the empirical sphaerosiderite $\delta^{18}O$ latitudinal gradient. Run 6 simulates extremely high relative humidity over the latitudinal transect and results in a siderite $\delta^{18}O$ gradient that is enriched by 1–2‰ relative to the empirical gradient.

### 5.2. Marine source water $\delta^{18}O$ compositions

The model was tested to see how changes in the latitudinal distribution of marine $\delta^{18}O$ compositions in the Cretaceous Western Interior Seaway (KWIS) might affect the latitudinal gradient in meteoric siderite $\delta^{18}O$ compositions. The model was first tested with a constant $\delta^{18}O$ composition for the KWIS that was set at $-1.2$‰, assuming no polar cryosphere (Shackleton and Kennett, 1975) and no evaporative enrichment of ocean surface waters. Runs 2–6 (Fig. 6C,D) were simulations in which the marine surface water $\delta^{18}O$ compositions were varied with latitude. The curves were not randomly generated. Some were set to simulate evaporative enrichment in the tropics coupled with freshwater mixing and subsequent depletion of the KWIS surface waters in the middle latitudes (Runs 2–4, Fig. 6C,D). Other simulations (Runs 5 and 6) were intended to test the model sensitivity to more extreme, unrealistic changes (i.e. highly depleted or highly enriched KWIS surface water $\delta^{18}O$ compositions). In all cases, the siderite $\delta^{18}O$ gradient shifted only 1–3‰ away from the best-fit gradient (Run 1). Extreme enrichments of the marine source water $\delta^{18}O$ compositions in the tropics enriched the siderite $\delta^{18}O$ gradient by 2–3‰ (Run 3), while extreme depletions in the marine source water $\delta^{18}O$ compositions (Run 5) depleted the siderite $\delta^{18}O$ gradient by approximately 3‰.

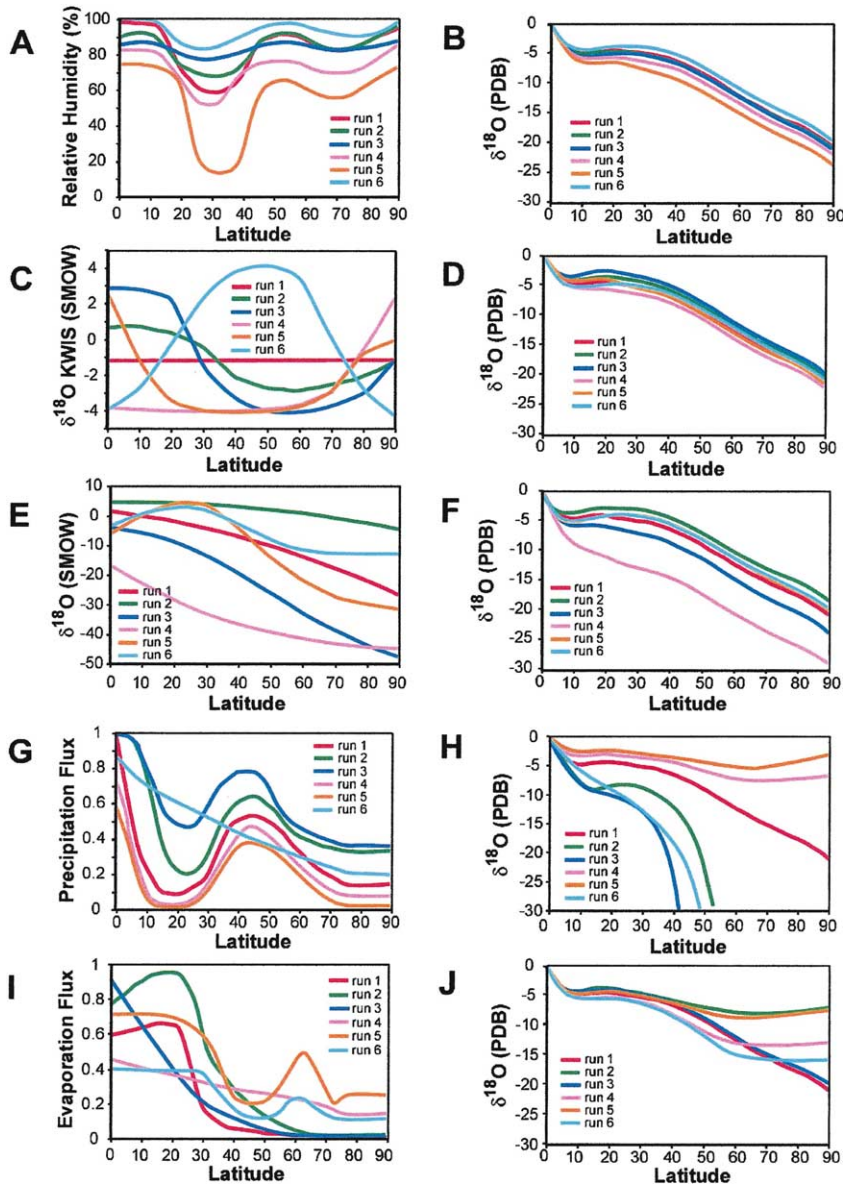


Fig. 6. Sensitivity tests were performed to determine how each of the model input parameters affected the model outputs. In each of the tests, 'Run 1' illustrates the best-fit Albian meteoric siderite $\delta^{18}O$ latitudinal gradient (right column, graphs B, D, F, H, and J), and the associated input parameters are illustrated in the left column (graphs A, C, E, G, and I). Six 'runs' were performed, where each variable was tested and the remaining variables were held constant at the 'Run 1' settings. The results of sensitivity tests on relative humidity are illustrated in graphs A and B, marine source water $\delta^{18}O$ compositions in graphs C and D, terrestrial source water $\delta^{18}O$ compositions in graphs E and F, precipitation flux in graphs G and H, and evaporation flux in graphs I and J.

### 5.3. Continental source water $\delta^{18}O$ compositions

The continental source water $\delta^{18}O$ compositions were initially modeled to have compositions very similar to the latitudinal distribution of calculated precipitation $\delta^{18}O$ values. This input parameter can be varied, however, and was tested to determine how different feedback compositions

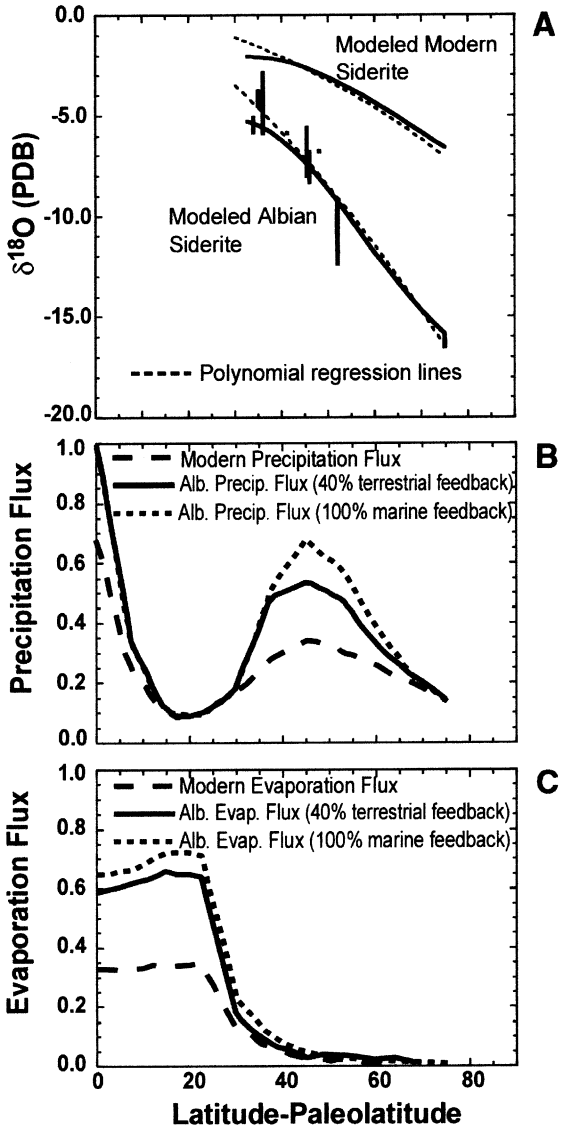


Fig. 7. (A) Modeled latitudinal gradients for the modern and Albian data sets (60% marine, 40% terrestrial vapor feedback simulation). The Albian data are only constrained over the latitudinal range 34–75°N. (B) the modeled latitudinal distributions of precipitation flux that generated the modern and Albian gradients in A. The modeled Albian precipitation flux is 38–52% greater than the modern. (C) Modeled latitudinal distributions of evaporation feedback flux (Albian 76–96% greater). The fluxes are the ratio of vapor added to or removed from the air mass vapor which had an initial dimensionless volume arbitrarily set at 1.

affected the model outputs (Fig. 6E,F). Run 1 represents the terrestrial source water isotopic compositions that best simulate the empirical sphaerosiderite $\delta^{18}O$ latitudinal gradient. The terrestrial source water gradient illustrated in Run 1 represents extrapolated, calculated water compositions from the empirical sphaerosiderite isotopic data. Run 2 simulates isotopically enriched terrestrial source waters and resulted in a siderite $\delta^{18}O$ gradient that is 3–4‰ enriched relative to the empirical siderite gradient. Run 3 simulates more depleted source water compositions and results in a siderite gradient that is 3–4‰ depleted relative to the empirical gradient. Run 4 simulates very depleted terrestrial source water isotopic compositions and results in a much more depleted siderite $\delta^{18}O$ gradient that is up to 10‰ lighter than the empirical gradient. Runs 5 and 6 both simulate isotopic enrichments in terrestrial source water compositions in the low latitude (20–35°N) dry belt regions. The terrestrial source water compositions drop off very steeply in Run 5 above 35°N latitude. In Run 6, the terrestrial source water gradient decreases gradually above 35°N and then becomes invariant (approximately −12.0‰) at 60°N latitude. Both Runs 5 and 6 result in a simulated siderite $\delta^{18}O$ gradient that is very similar (within 1–2‰) of the empirical sphaerosiderite $\delta^{18}O$ latitudinal gradient.

### 5.4. Precipitation flux

The dimensionless precipitation flux curves were modeled to have the same general latitudinal profile as the modern global distribution of precipitation rates (i.e. high precipitation in the tropics and mid-latitudes, low precipitation in the dry belts and high latitudes) (e.g. Barron et al., 1989; Gates et al., 1992). Changes in the precipitation flux curves result in significant changes in the simulated siderite $\delta^{18}O$ gradients. Run 1 represents the precipitation flux curve that results in a simulated $\delta^{18}O$ gradient that reproduces the empirical sphaerosiderite $\delta^{18}O$ latitudinal gradient (Fig. 6G,H). Run 1 is characterized by very high precipitation flux in the tropics, low precipitation flux in the low-latitude dry belt (20–30°N), high precipitation flux in the mid-latitudes, and low

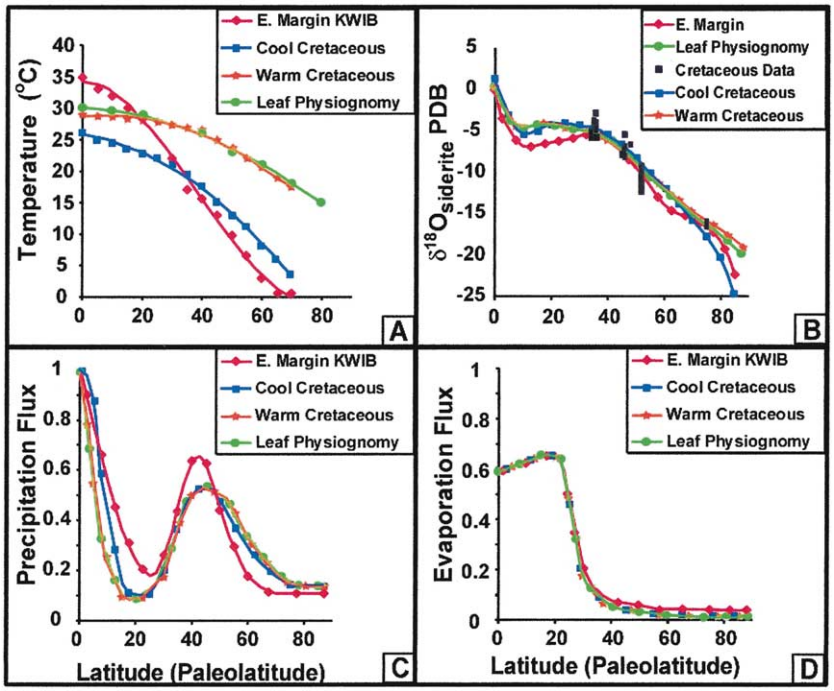


Fig. 8. (A) The four gradients illustrated represent the thermal gradients (with best-fit polynomial curves) that were embedded in the mass balance model to test temperature sensitivity. The warm and cool Cretaceous curves were obtained from Barron (1983), the E. Margin KWIB curve is from Poulsen et al. (1999), and the Leaf Physiognomy curve is from Wolfe and Upchurch (1987) (in Spicer and Corfield, 1992). (B) With each temperature gradient, it was possible to reproduce a latitudinal gradient that fits the Albian siderite $\delta^{18}O$ values. (C) Each curve represents the input precipitation flux profile that generates the siderite $\delta^{18}O$ gradient illustrated in B. (D) The input evaporation flux curves for each of the four tests are illustrated; however, only very minor changes were required in one of the tests (E. Margin KWIB temperature gradient).

precipitation flux in the high latitudes. Runs 2 and 3 represent simulations modeled with significantly higher precipitation fluxes than those of Run 1. In both cases (Runs 2 and 3), the resulting siderite $\delta^{18}O$ gradient becomes extremely steep and very highly depleted relative to the empirical gradient such that the model 'crashes' (exhausts the vapor reservoir) prior to reaching the high latitudes. Runs 4 and 5 represent simulations where the precipitation fluxes are significantly lower than those of Run 1. In these simulations (Runs 4 and 5), the resulting siderite $\delta^{18}O$ gradient is shallower, and isotopically enriched relative to the empirical sphaerosiderite $\delta^{18}O$ gradient. These simulations result in simulated $\delta^{18}O$ latitudinal gradients that become progressively enriched with increased latitude. Run 6 tests an overall (nearly linear) decrease in precipitation flux with increased latitude (Fig. 6G,H). In this scenario, the resultant siderite $\delta^{18}O$ gradient becomes extremely steep and highly depleted relative to the empirical sphaerosiderite $\delta^{18}O$ latitudinal gradient. The vapor reservoir is again exhausted before the simulated air masses reach high latitudes.

### 5.5. *Evaporation flux*

The dimensionless evaporation flux curves were modeled to roughly resemble modern equator-to-pole profiles of evaporation rates (e.g. Barron and Moore, 1994). Run 1 represents the evaporation flux curve that most closely reproduces the empirical Albian sphaerosiderite $\delta^{18}O$ latitudinal gradient. The curve (Run 1) is characterized by high evaporation flux in the tropics and low-latitude dry belt regions (20–30°N), and rapidly declines to very low evaporation flux values in the

higher latitudes (Fig. 6I,J). Run 2 simulates a significantly higher equator-to-pole evaporation flux curve (relative to Run 1). The resultant siderite $\delta^{18}O$ gradient closely resembles the empirical sphaerosiderite $\delta^{18}O$ gradient in the low latitudes; however, the simulated gradient is shallower and isotopically enriched relative to the empirical gradient above 40°N latitude. Run 3 simulates an exponential decrease in the hemispherical distribution of evaporation flux, and the resultant simulated siderite $\delta^{18}O$ gradient closely reproduces the empirical Albian sphaerosiderite $\delta^{18}O$ latitudinal gradient. Run 4 simulates a steady decline in the equator-to-pole distribution of evaporation flux with lowered values relative to Run 1 in the low latitudes, and higher values in the mid to high latitudes. The resultant siderite $\delta^{18}O$ gradient is 2–3‰ depleted relative to the empirical Albian sphaerosiderite $\delta^{18}O$ gradient below 60°N latitude and enriched relative to the empirical gradient by up to 8–10‰ in the high latitudes. Run 5 simulates overall increased evaporation fluxes relative to Run 1. Run 5 has higher evaporation fluxes in the low latitudes up to 40°N and includes another peak in evaporation flux values between 55 and 75°N latitude. The resultant siderite $\delta^{18}O$ gradient closely resembles the empirical sphaerosiderite $\delta^{18}O$ gradient up to approximately 45°N latitude; however, it then becomes flattened and isotopically enriched beyond 60°N latitude. Run 6 simulates lowered evaporation flux values (relative to Run 1) in the low latitudes (0–30°N); however, it has higher evaporation fluxes in the mid to high latitudes (relative to Run 1) and also includes a second peak in evaporation flux values between 55 and 70°N latitude. The resultant simulated siderite $\delta^{18}O$ gradient is 3–4‰ depleted relative to the empirical Albian sphaerosiderite $\delta^{18}O$ gradient up to approximately 55°N latitude, where the curve then flattens abruptly and becomes isotopically invariant at approximately −16.0‰ up to 90°N latitude.

Varying the proportion of terrestrial- and marine-sourced vapor feedback to the evolving air masses further tested the model sensitivity. Since our mass balance model tracks the evolving isotopic composition of atmospheric moisture in air masses moving through an epicontinental seaway (KWIS), using a coastal plain proxy record (sphaerosiderites), it is probable that much of the vapor feedback was from marine source water. The model was tested with between 0% and 40% terrestrially sourced water vapor (Fig. 7B,C). Both the extreme end-member conditions (60% and 100% marine-derived vapor) require significant increases in both the Albian precipitation and evaporation fluxes relative to the fluxes needed to replicate the modern (theoretical) siderite $\delta^{18}O$ gradient (Fig. 7B,C). In the simulations with the largest terrestrial evaporation flux (40% of total vapor feedback) a 34% increase in the precipitation flux and a 76% increased evaporation flux (over the modern fluxes) (Fig. 7B,C) was needed to accurately reproduce the Albian siderite $\delta^{18}O$ latitudinal gradient (Fig. 7A). In the end-member simulation of 100% marine-derived water vapor, the calculated precipitation and evaporation fluxes increased to 52% and 96%, respectively.

### 5.6. Temperature

Several predicted mid-Cretaceous temperature gradients were used to test the model sensitivity to variations in temperature. Our primary source of data was the empirical temperature gradient of Wolfe and Upchurch (1987), which is based upon fossil terrestrial vegetation (leaf physiognomy) (Spicer and Corfield, 1992). Our intention was to use empirical temperature data independent of the sphaerosiderite proxy to calibrate the model rather than theoretical estimates. We did, however, further test the model sensitivity to variations in predicted mid-Cretaceous thermal gradients using temperature predictions produced by GCM modeling experiments. Tests were performed using both the warm and cool Cretaceous temperature range limits specified by Barron (1983) and the eastern margin KWIB temperature gradient generated from the AGCM experiments of Poulsen et al. (1999).

During each test, all variables were held constant except for the precipitation fluxes. With each temperature gradient, a unique profile of precipitation flux was generated with latitude (Fig. 8). In all cases, an increase in precipitation flux was

necessary (compared to the modern profile) to reproduce the empirical Albian siderite $\delta^{18}O$ values. A 34% increase in overall precipitation flux relative to the modern precipitation flux curve was necessary to reproduce the Albian siderite $\delta^{18}O$ values using the empirical temperature gradient of Wolfe and Upchurch (1987). With the warm Cretaceous temperature gradient of Barron (1983), a 32% increase in overall precipitation flux is necessary. The cool Cretaceous gradient of Barron (1983) requires a 41% increase, and the E. Margin KWIB gradient of Poulsen et al. (1999) requires a 59% increase in precipitation flux. In all cases, the greatest increases in the Cretaceous precipitation flux profiles relative to the modern profile occur in the tropical latitudes (0–15°N) and the middle latitudes (35–60°N) (Fig. 8).

## 6. Discussion

### 6.1. Implications of sensitivity experiments

Experiments involving changes in the Cretaceous temperature curves show that the model is very sensitive to changes in the thermal gradient. Each temperature curve required significant changes in the precipitation flux profiles. The cooler temperature gradients of Barron (1983) and Poulsen et al. (1999) require greater increases in precipitation flux. However, the increased precipitation fluxes required from these cooler temperature gradients do not equate to increased precipitation rates (see discussion below). The temperature sensitivity tests, particularly the cooler gradients, show that increased precipitation fluxes are indeed necessary to reproduce our Albian siderite $\delta^{18}O$ values.

The model is moderately sensitive to changes in the equator-to-pole relative humidity curve. The empirical sphaerosiderite $\delta^{18}O$ latitudinal gradient is best replicated with high relative humidity values with an average equator-to-pole relative humidity of 80–85%. Very low average equator-to-pole relative humidity values shift the entire gradient to more depleted isotopic compositions (negative 3–4‰ shift). Extremely high average relative humidity values shift the simulated siderite $\delta^{18}O$ gradient to slightly more enriched isotopic compositions (positive 1–2‰ shift). The positive and negative shifts in the modeled $\delta^{18}O$ precipitation gradient (and consequently the modeled siderite $\delta^{18}O$ gradient) agree well with the kinetic isotope effects of humidity upon evaporating seawater forming water vapor (Gonfiantini, 1986), illustrated in Clark and Fritz (1997, p. 44).

Changes in the isotopic composition of the oceanic source waters had little effect upon the modeled siderite $\delta^{18}O$ gradients. Variations in the KWIS and Tethyan source water compositions were modeled with surface water $\delta^{18}O$ compositional trends similar to the profiles of the modern GEOSECS transects in the Pacific and Atlantic Oceans (Broeker, 1989) (Run 2, Fig. 6D). These variations caused only slight changes in the model outputs and actually yielded a simulated siderite $\delta^{18}O$ gradient that closely resembles the empirical gradient. Other simulations (Runs 3 and 5, Fig. 6D) were prompted by modeled circulation patterns in the KWIS (Slingerland et al., 1996). These simulations shifted the gradient slightly ($\pm 2$‰), yet still produced very similar results. Even highly depleted (Run 4, Fig. 6C) and highly enriched (Run 6, Fig. 6C) marine source water $\delta^{18}O$ compositions yielded simulated siderite $\delta^{18}O$ gradients similar to the empirical gradient (Fig. 6D). Thus, we interpret that latitudinal changes in the marine source water compositions had only minor effects upon the Albian $\delta^{18}O$ precipitation gradients.

The model is very sensitive to changes in the equator-to-pole trends in the collective isotopic composition of terrestrial source waters. There is positive correlation in that enrichment or depletion of the terrestrial source water $\delta^{18}O$ compositions results in enrichment or depletion, respectively, of the modeled siderite $\delta^{18}O$ latitudinal gradient. The isotopic composition of terrestrial source water feedback to air masses is a very difficult parameter to quantify in the modern and more so in the ancient. The model best replicates the empirical sphaerosiderite $\delta^{18}O$ latitudinal gradient when the terrestrial source water isotopic compositions are set to the precipitation $\delta^{18}O$ values calculated from the empirical sphaerosiderite data and the warm-Cretaceous temperature gradient of Wolfe and Upchurch (1987).

The model is most sensitive to changes in the precipitation and evaporation fluxes. This was true for both the modern and Albian model simulations. Exceedingly high evaporative feedback causes the modeled siderite $\delta^{18}O$ gradient to become exponentially enriched with increased latitude. Conversely, with very low amounts of evaporative feedback the vapor reservoir is exhausted before the air mass reaches polar latitudes. Similarly, exceedingly high amounts of precipitation flux drain the vapor reservoir and low precipitation fluxes result in a siderite $\delta^{18}O$ gradient that becomes increasingly enriched. Only a narrow range of precipitation and evaporation fluxes can simulate the modern and Albian siderite $\delta^{18}O$ gradients (Fig. 7).

Under all modeled conditions evaporative feedback increased substantially at all latitudes in the Albian simulations and exhibits a maximum that coincides with that in modern simulations ($\sim$30°N). The precipitation flux requires moderate increases at low latitudes and little to no changes in the dry belts (20–30°N). Quite notably, the latitudes of maximum precipitation are consistent with those of modern simulations (0–15°N and 35–55°N latitude); however, the Albian fluxes increase by 40–100% of the modern flux in those latitudes, respectively (Fig. 7B). The large increases in evaporation flux (76–96%) are likely a result of the increased moisture capacity of a warmer Cretaceous atmosphere (Barron et al., 1989). Late Cretaceous (Campanian) climate model simulations suggest the amount of precipitable water in the atmosphere was 2× present-day values (Hay and DeConto, 1999). Based upon the Clausius–Clapeyron relationship between temperature and saturation vapor pressure, the amount of vapor that can be held in the atmosphere nearly doubles with every 10°C increase in temperature.

### 6.2. Precipitation rate calculations

The dimensionless precipitation and evaporation fluxes helped to simplify the mass balance model; however, it is much more meaningful to convert the model fluxes into rates. We estimated maximum coastal precipitation rates throughout the KWIB from modern precipitation rate data, the model fluxes, and the relationship between temperature and saturation vapor pressure. Saturation vapor pressure (g/m$^3$) is described in terms of temperature by the exponential expression:

$$0.0002T^3 + 0.0111T^2 + 0.321T + 4.8 \quad \text{(Clark and Fritz, 1997)} \tag{3}$$

Saturation vapor pressure curves were computed from the modern and warm Cretaceous latitudinal temperature gradients so that the difference in modern vs. Albian potential saturation vapor pressures can be determined at any latitude (Fig. 9). Precipitation rates are determined at individual latitudes through the following algebraic expressions:

$$P_m/F_m = H_m \tag{4}$$

$$\Delta VP_{k-m} = (VP_k - VP_m)/(VP_m)$$

$$(1 + \Delta VP_{k-m})H_m = H_k$$

$$H_k F_k = P_k$$

where $P$ = precipitation rate in mm/yr; $F$ = di-

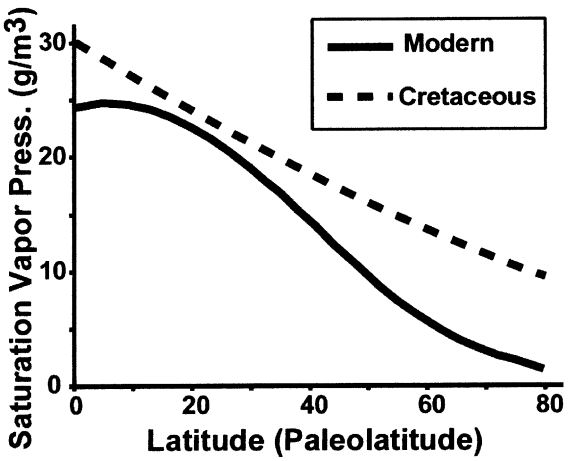


Fig. 9. The curves represent latitudinal gradients in air mass saturation vapor pressures calculated from the modern and warm-Cretaceous latitudinal temperature gradients illustrated in Fig. 1. The saturation vapor pressures are calculated using the equation of Clark and Fritz (1997).

mensionless yearly flux (i.e. rate constant); $H$ = height of infinitesimally small water column $p$; $\Delta VP$ = the change in potential saturation vapor pressures; and the subscript m = modern, k = Cretaceous. It should be noted that the saturation vapor pressures are completely temperature-dependent. Our calculations are based upon the temperature gradients embedded in the model, the precipitation flux profiles generated using those temperature gradients, and modern average precipitation rates for that particular latitude.

Our calculations indicate that the warm Cretaceous atmosphere (on average) may have had a vapor capacity 93% greater than present. The vapor-holding capacity of the warm Cretaceous atmosphere was significantly greater in mid to high latitudes, where temperatures were significantly warmer than present (Fig. 2). For example, at 45°N latitude the vapor-holding capacity of the Cretaceous atmosphere was potentially 147% greater than present. At 45°N latitude there is a 60–100% increase in Albian precipitation flux. Presently, the average precipitation rate at 45°N is 2.3 mm/day (840 mm/yr) (Barron et al., 1989; Gates et al., 1990). Our precipitation rate calculations imply Albian mid-latitude (45°N) precipitation rates on the order of 7.2 mm/day (2618 mm/yr), up to 9.0 mm/day (3297 mm/yr) (Table 3). At high paleolatitudes (75°N), the vapor-holding capacity of the Cretaceous atmosphere was potentially 450% greater than present. Current average precipitation rates at 75°N latitude are on the order of 0.75 mm/day (275 mm/yr). Based upon our calculations, Albian precipitation rates at 75°N were on the order of 4.1 mm/day (1500 mm/yr).

At mid-latitudes, Community Climate Model (CCM) simulations (Barron et al., 1989) suggest a 40% increase in northern hemisphere precipitation rates. GENESIS modeling of the mid-Cretaceous world suggests a doubling of high-latitude precipitation rates, and mid-latitude precipitation rates ranged from approximately 3 to 6 mm/day (1100–2200 mm/yr) (maximum 140% increase) (Poulsen et al., 1999). With the temperature gradient of Poulsen et al. (1999) embedded in our mass balance model, we get results that are in close agreement with (approximately 800–1600 mm/yr) AGCM predictions for the same latitudes. Our precipitation rate calculations that are based upon the empirical temperature gradient of Wolfe and Upchurch (1987) are similar to those generated using the warm Cretaceous temperature gradient of Barron (1983) in the low latitudes (0–30°N), and somewhat lower in the mid to higher latitudes (Fig. 10). Using the cool Cretaceous temperature gradient of Barron (1983), our calculations predict significantly higher precipitation rates (compared to modern rates) in the tropics, but only slightly higher precipitation rates in the mid to high latitudes.

White et al. (2001) suggest mid-latitude precipitation rates ranged from 1300 to 3200 mm/yr and may have reached as high as 4100 mm/yr along the eastern margin of the KWIB (44–250% increase). The mid-latitude calculations of White et al. (2001) are higher than those presented here (2618–3297 mm/yr). White et al. (2001) based

Table 3
Mid-Cretaceous precipitation rates were calculated from experiments with the mass balance model

| Latitude | MAT (°C) | Sat. $VP$ (g/m$^3$) | Precipitation flux | Calculated precipitation rate (mm/yr) | Source of temperature data |
|---|---|---|---|---|---|
| 45°N | 11.5 | 10.3 | 0.34 | 840 | IAEA/WMO (present precipitation rate and MAT) |
| 45°N | 15.0 | 12.8 | 0.53 | 1632 | Barron, 1983 (cool Cretaceous) |
| 45°N | 25.0 | 22.9 | 0.54 | 2965 | Barron, 1983 (warm Cretaceous) |
| 45°N | 13.0 | 11.3 | 0.63 | 1712 | Poulsen et al., 1999 (E. Margin KWIB) |
| 45°N | 19.9 | 17.2 | 0.54 | 2618 | Wolfe and Upchurch, 1987 (Cretaceous Leaf Physiognomy) |

Several different temperature gradients (including the modern) were embedded in the model, and a unique precipitation flux profile was generated for each test. Saturation vapor pressures were also calculated from the MATs. Using Eq. 4 (see text), precipitation rate (mm/yr) estimates for 45°N paleolatitude were calculated from each modeling experiment.

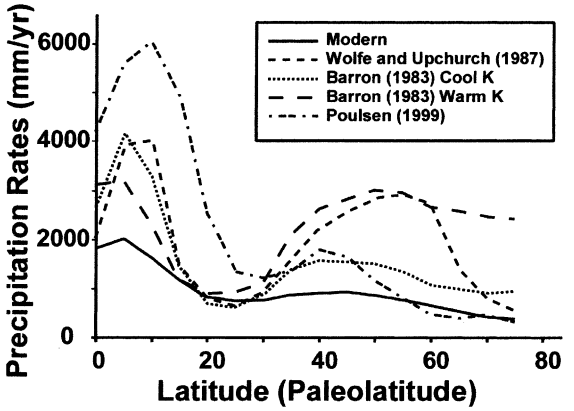


Fig. 10. Precipitation rates (estimates) were determined from each of the four mid-Cretaceous temperature gradients used in the modeling experiments (Barron, 1983; Poulsen et al., 1999; Wolfe and Upchurch, 1987). The latitudinal distribution of our mid-Cretaceous precipitation rate estimates is compared to a modern profile of northern hemisphere (continental) precipitation rates.

their calculations upon modern empirical amount effect relationships (Dansgaard, 1964) and linear slope comparisons between a subset of the Albian empirical sphaerosiderite data (35–52°N paleolatitude) and a subset of the IAEA/WMO data over the same latitudinal range. With the additional high paleolatitude sphaerosiderite data presented in this study, however, it is clear that the slopes of the modern and Albian siderite $\delta^{18}O$ gradients are distinctly different and the technique used by White et al. (2001) cannot be applied to a broader range of paleolatitudes.

## 7. Conclusions

The mass balance model confirms our initial hypothesis concerning a more active hydrologic cycle during the Albian, and now allows us to quantify KWIB coastal precipitation rates. Our estimates indicate mid-latitude, coastal precipitation rates on the order of 2600–3300 mm/yr in the KWIB, and high paleolatitude (North Slope, Alaska) coastal precipitation rates on the order of 560 mm/yr. The sphaerosiderite $\delta^{18}O$–paleolatitudinal gradient and modeling experiments presented here stress the need for continental stable isotopic proxy records to quantify changes in the hydrologic cycle during 'greenhouse world' climates. The modern temperature–precipitation $\delta^{18}O$ relationship, as well as other modern climate-dependent empirical relationships may not be valid under different climate modes, especially warm equable periods (Koch et al., 1995). Independent paleoprecipitation $\delta^{18}O$ and paleotemperature proxy records should be used for paleoclimatic reconstructions and model validation (Fricke and O'Neil, 1999).

## Acknowledgements

This project was supported by NSF Grant #EAR 96-28128 and by the University of Iowa Center for Global and Regional Environmental Research. A Geological Society of America research grant, and department of education GAANN fellowship supported D.F.U. Thanks to Dr. Dale Leckie and Dr. Paul McCarthy for donating some of the core samples used in this study. We would especially like to thank Dr. Chris Poulsen and Dr. Walter Dean for their constructive reviews of this manuscript. Thanks also to T. White, K. Saville, L. Young, P.L. Phillips, S.J. Carpenter, L. Wingate and K.C. Lohmann.

## References

Barron, E.J., 1983. Warm equable Cretaceous, The nature of the problem. Earth Sci. Rev. 19, 305–338.

Barron, E.J., Hay, W.W., Thompson, S., 1989. The hydrologic cycle: a major variable during Earth history. Paleogeogr. Paleoclimatol. Palaeoecol. 75, 157–174.

Barron, E.J., Peterson, W.H., 1990. Mid-Cretaceous ocean circulation: Results from model sensitivity studies. Paleoceanography 5, 319–337.

Barron, E.J., Moore, G.T., 1994. Climate Model Applications in Paleoenvironmental Analysis. SEPM Short Course 33, Tulsa, OK, 339 pp.

Barron, E.J., Fawcett, P.J., Pollard, D., Thompson, S., 1993. Model simulations of Cretaceous climates: the role of geography and carbon dioxide. Phil. Trans. R. Soc. London B 341, 307–316.

Barron, E.J., Fawcett, P.J., Peterson, W.H., Pollard, D., Thompson, S.L., 1995. A 'simulation' of Mid-Cretaceous climate. Paleoceanography 10, 953–962.

Bardossy, G., 1982. Karst Bauxites: Bauxite Deposits on Carbonate Rocks. Elsevier, Amsterdam, 441 pp.

Brenner, R.L., Ludvigson, G.A., Witzke, B.J., Zawistoski, A.N., Kvale, E.P., Ravn, R.L., Joekel, R.M., 2000. Late Albian Kiowa-Skull Creek transgression, lower Dakota Formation, eastern margin of Western Interior Seaway. J. Sediment. Res. 70, 868–878.

Broeker, W.S., 1989. The salinity contrast between the Atlantic and Pacific Oceans during glacial time. Paleoceanography 4, 207–212.

Carothers, W.W., Lanford, H.A., Rosenbauer, R.J., 1988. Experimental oxygen isotope fractionation between siderite-water and phosphoric acid liberated $CO_2$-siderite. Geochim. Cosmochim. Acta 52, 2445–2450.

Clark, I., Fritz, P., 1997. Environmental Isotopes in Hydrogeology. Lewis, Boca Raton, FL.

Dansgaard, W., 1964. Stable isotopes in precipitation. Tellus 16, 436–468.

Dansgaard, W., Clausen, H.B., Gundestrup, N., Hammer, C.U., Johnsen, S.J., Kristinsdottir, P., Reeh, N., 1973. Stable isotope glaciology. Medd. Grønland 2, 1–53.

Dettman, D.L., Lohman, K.C., 2000. Oxygen isotope evidence for high-altitude snow in Laramide Rocky Mountains of North America during the Late Cretaceous and Paleogene. Geology 28, 243–246.

Fricke, H.C., O'Neil, J.R., 1999. The correlation between $^{18}O/^{16}O$ ratios of meteoric water and surface temperature: its use in investigating terrestrial climate change over geologic time. Earth Planet. Sci. Lett. 170, 181–196.

Gates, W.L., Rowntree, P.R., Zeng, Q.C., 1990. Validation of climate models. In: Houghton, J.T., Jenkins, G.J., Ephraums, J.J. (Eds.), Climate Change: The IPCC Scientific Assessment. Cambridge University Press, Cambridge, pp. 92–130.

Gates, W.L., Mitchell, J.F.B., Boer, G.J., Cubasch, U., Meleshko, V.P., 1992. Climate modeling, climate prediction, and model validation. In: Houghton, J.T., Callander, B.A., Varney, S.K. (Eds.), Climate Change 1992, The Supplementary Report to the IPCC Scientific Assessment. Cambridge University Press, Cambridge, pp. 97–134.

Gonfiantini, R., 1986. Environmental isotopes in lake studies. In: Fritz, P., Fontes, J.Ch. (Eds.), Handbook of Environmetal Isotope Geochemistry, vol. 2, The Terrestrial Environment, B. Elsevier, Amsterdam, pp. 113–168.

Hay, W.W., DeConto, R.M., 1999. Comparison of modern and Late Cretaceous meridional energy transport and oceanology. In: Barrera, E., Johnson, C.C. (Eds.), Evolution of the Cretaceous Ocean-Climate System, Geol. Soc. Am. Spec. Pap. 332, pp. 73–90.

Hays, P.D., Grossman, E.L., 1991. Oxygen isotopes in meteoric calcite cements as indicators of continental paleoclimate. Geology 19, 441–444.

Koch, P.L., Zachos, J.C., Dettman, D.L., 1995. Stable isotope stratigraphy and paleoclimatology of the Paleogene Bighorn Basin (Wyoming, USA). Palaeogeogr. Palaeoclimatol. Palaeoecol. 115, 61–89.

Liu, B., Phillips, F.M., Hoines, S., Campbell, A.R., Sharma, P., 1995. Water movement in desert soils traced by hydrogen and oxygen isotopes, chloride, and chlorine-36, southern Arizona. J. Hydrol. 168, 91–110.

Lohmann, K.C., 1988. Geochemical patterns of meteoric diagenetic systems and their application to studies of paleokarst. In: James, N.P., Choquette, P.W. (Eds.), Paleokarst, Springer, pp. 58–80.

Ludvigson, G.A., Gonzalez, L.A., Metzger, R.A., Witzke, B.J., Brenner, R.L., Murillo, A.P., White, T.S., 1998. Meteoric sphaerosiderite lines and their use for paleohydrology and paleoclimatology. Geology 26, 1039–1042.

Majoube, M., 1971. Fractionnement en oxygène-18 et en deutérium entre l'eau et as vapeur. J. Chem. Phys. 197, 1423–1436.

McCarthy, P.J., Martini, I.P., Leckie, D.A., 1997. Pedosedimentary history and floodplain dynamics of the Lower Cretaceous upper Blairmore Group, southwestern Alberta, Canada. Can. J. Earth Sci. 34, 598–617.

Mitchell, J.B.F., Manabe, S., Tokioka, T., Meleshko, V., 1990. Equilibrium climate change. In: Houghton, J.T., Jenkins, G.J., Ephraums, J.J. (Eds.), Climate Change: The IPCC Scientific Assessment. Cambridge University Press, Cambridge, pp. 131–172.

NOAA, 2001. COADS Release 1, mean relative humidity. http://www.cdc.noaa.gov/coads/RH.html.

Poulsen, C.J., Barron, E.J., Johnson, C., Fawcett, P., 1999. Links between major climatic factors and regional oceanic circulation in the mid-Cretaceous. In: Barrera, E., Johnson, C.C. (Eds.), Evolution of the Cretaceous Ocean-Climate System, Geol. Soc. Am. Spec. Pap. 332, pp. 73–90.

Price, G.D., Valdes, P.J., Sellwood, B.W., 1998. A comparison of GCM simulated 'greenhouse' and 'icehouse' climates: implications for the sedimentary record. Palaeogeogr. Palaeoclimatol. Palaeoecol. 142, 123–138.

Rozanski, K., Araguas-Araguas, L., Gonfiantini, R., 1993. Isotopic patterns in modern global precipitation. In: Swart, P.K., Lohmann, K.C., McKenzie, J., Savin, S. (Eds.), Climate Change in Continental Isotopic Records. Amer. Geophys. Union Geophys. Mono. 78, pp. 1–36.

Scotese, C.R., 1991. Jurassic and Cretaceous plate tectonic reconstructions. Paleogeogr. Paleoclimatol. Paleoecol. 87, 493–501.

Shackleton, N.J., Kennett, J.P., 1975. Late Cenozoic oxygen and carbon isotopic changes at DSDP site 284: implications for glacial history of the Northern Hemisphere. In: Kennett, J.P., Houtz, R.E., et al. (Eds.), Init. Rep. DSDP 29, pp. 801–807.

Sigleo, W., Reinhardt, J., 1988. Paleosols from some Cretaceous environments in the southeastern United States. In: Reinhardt, J., Sigleo, W.R. (Eds.), Paleosols and Weathering through Geologic Time: Principles and Applications. Geol. Soc. Am. Spec. Pap. 216, pp. 123–142.

Slingerland, R., Kump, L.R., Arthur, M.A., Faucett, P.J., Sageman, B., Barron, E.J., 1996. Estuarine circulation in the Turonian Western Interior Seaway of North America. Geol. Soc. Am. Bull. 108, 941–952.

Spicer, R.A., Corfield, R.M., 1992. A review of terrestrial and marine climates in the Cretaceous with implications for

modeling the 'Greenhouse Earth'. Geol. Mag. 129, 169–180.

Ufnar, D.F., Gonzalez, L.A., Ludvigson, G.A., Brenner, R.L., Witzke, B.J., 2001. Stratigraphic implications of meteoric sphaerosiderite $\delta^{18}O$ compositions in paleosols of the Cretaceous (Albian) Boulder Creek Formation, NE British Columbia Foothills, Canada. J. Sediment. Res. 71, 1017–1028.

White, T.S., Witzke, B.J., Ludvigson, G.A., Brenner, R.L., Gonzalez, L.A., Ravn, R.L., 2000a. The paleoclimatological significance of Albian (mid-Cretaceous) sphaerosiderites from eastern Saskatchewan and western Manitoba, Summary of investigations 2000, vol. 1. Saskatchewan Geol. Survey Misc. Rep. 2000-4.1, pp. 63–75.

White, T.S., Witzke, B.J., Ludvigson, G.A., 2000b. Evidence for an Albian Hudson Arm of the North American Cretaceous Western Interior Seaway. Geol. Soc. Am. Bull. 112, 1342–1355.

White, T.S., Gonzalez, L.A., Ludvigson, G.A., Poulsen, C., 2001. The mid-Cretaceous hydrologic cycle of North America. Geology 29, 363–366.

Witzke, B.J., Ludvigson, G.A., 1996. Coarse-grained facies. In: B.J. Witzke, G.A. Ludvigson (Eds.), Mid-Cretaceous Fluvial Deposits of the Eastern Margin, Western Interior Basin: Nishnabotna Member, Dakota Formation. Iowa Department of Natural Resources Geological Survey Bureau Guidebook Series No. 17, pp.19–30.

Wolfe, J.A., Upchurch, G.R., Jr., 1987. North American nonmarine climates and vegetation during the Late Cretaceous. Paleogeogr. Paleoclimatol. Paleoecol. 61, 33–77.

Yurtsever, Y., Gat, J.R., 1981. Atmospheric waters. In: Gat, J.R., Gonfiantini, R. (Eds.), Stable Isotope Hydrology: Deuterium and Oxygen-18 in the Water Cycle. IAEA Technical Reprint Series 210, pp. 103–142.

Zheng, Y.-F., 1999. Oxygen isotope fractionation in carbonate and sulfate minerals. Geochem. J. 33, 109–126.